Journal of Materials Chemistry A

Strain-modified ionic conductivity in rare-earth substituted ceria: Effects of migration direction, barriers, and defect-interactions

Journal:	*Journal of Materials Chemistry A*
Manuscript ID	TA-ART-12-2020-012150.R1
Article Type:	Paper
Date Submitted by the Author:	03-Mar-2021
Complete List of Authors:	Harrington, George; Kyushu University, Next-Generation Fuel Cell Research Centre (NEXT-FC); Massachusetts Institute of Technology, Materials Engineering and Science; Kyushu University, Center of Coevolutionary Research for Sustainable Communities (C2RSC); Kyushu University, International Institute for Carbon Neutral Energy Research (I2CNER) Kim, Sunho; Massachusetts Institute of Technology, Department of Materials Engineering and Science Sasaki, Kazunari; Kyushu University, Next-Generation Fuel Cell Research Centre (NEXT-FC); Kyushu University, Center of Coevolutionary Research for Sustainable Communities (C2RSC); Kyushu University, International Institute for Carbon Neutral Energy Research (I2CNER) Tuller, Harry; Massachusetts Institute of Technology, Department of Materials Science and Engineering; Kyushu University, International Institute for Carbon Neutral Energy Research (I2CNER) Grieshammer, Steffen; Forschungszentrum Jülich GmbH, Helmholtz-Institut Münster; RWTH Aachen University, Institute of Physical Chemistry

ARTICLE

Strain-modified ionic conductivity in rare-earth substituted ceria: Effects of migration direction, barriers, and defect-interactions

Received 00th January 20xx,
Accepted 00th January 20xx

DOI: 10.1039/x0xx00000x

George F. Harrington[*a,b,c,d], Sunho Kim[d], Kazunari Sasaki[a,b,c], Harry Tuller[d,c], and Steffen Grieshammer[*e,f,g]

It is crucial to understand how ionic transport in functional oxides is affected by strain, which may unintentionally occur during the fabrication or operation of electrochemical devices or may be intentionally engineered for improved functional properties. In this work, the change in ionic conductivity of biaxially strained epitaxial films of rare-earth substituted ceria was measured. By thermally annealing strained epitaxial films, the strain state was varied, and the conductivity was extracted without contributions from grain boundaries. It is shown that transport in the out-of-plane direction, with respect to the strained axes, is more sensitive to the strain state than in the in-plane direction. In addition, the size of the rare-earth substitutionals significantly impacts the extent of the strain effect on the ionic conductivity. The conductivity was simulated by the Kinetic Monte Carlo method based on energies from density functional theory to deconvolute the effects of strain on the migration barriers and defect interactions. It was revealed that both the barriers and interactions contribute to the strain-modified transport, however, it is important to take into account the long-range motion rather than individual barriers and interactions. These findings provide new generalized insights into how strain affects ionic transport in crystalline materials, which may lead to a more sophisticated approach to engineering functional oxides.

1 Introduction

Investigating the impact of lattice strain and exploring the potential of strain-engineering has, in recent years, become a critical component in the development of functional oxides for applications such as solid oxide fuel/electrolyser cells,[1] memristors,[2] catalysis[3], Li-ion batteries[4], and sensors.[5] Reported examples of strain-modified properties include altered ionic conductivity,[6–8] increased surface exchange,[9,10] reduced cation segregation,[11,12] tuning of non-stoichiometry,[13,14] and phase stabilization.[15] Of these, strain-modified ionic conductivity was the first to attract widespread attention,[16,17] and has since been one of the most studied, in particular in fluorite structured ZrO_2- and CeO_2-based solid-state solutions.[18] Despite over a decade of research, however, the reproducible preparation and measurement of strained structures is an unresolved challenge preventing the establishment of a general consensus on the quantitative relation between strain and ionic conductivity. Furthermore, a detailed description of the relation between strain and the long-range motion of ions is yet to be established. As such, both reliable experimental data as well as detailed theoretical insights into strain effects are vital for a comprehensive description of strain modified transport and for exploiting strain-engineering of functional oxides for electrochemical devices.

In acceptor-substituted fluorite-structured oxides, such as yttria stabilized zirconia or rare-earth- substituted ceria (RE:CeO_2), where the oxygen vacancy concentration is fixed by the acceptor concentration, ion migration occurs by an oxygen vacancy hopping mechanism, and the conductivity can be expressed by

$$\sigma = \frac{\sigma_0}{T} \exp\left(-\frac{\Delta E_{mig}}{k_B T}\right) \qquad (1)$$

where ΔE_{mig} is the activation energy of migration and the pre-exponential term, σ_0, contains the charge and concentration of vacancies, the jump distance, the jump attempt frequency, geometric factors, and entropic terms.[19] Generally, it is expected that strain mainly affects the exponent, ΔE_{mig}, such that tensile strain reduces the migration energy and increases the conductivity, and compressive strain increases the barriers and diminishes the conductivity. Changes to the components of the pre-exponential term with strain are likely to be trivial in comparison and have a limited influence on the conductivity.[6,20]

Computational studies on strained oxygen ion conductors have predominantly focused on the migration edge energies, the height of

[a] Next-Generation Fuel Cell Research Centre (NEXT-FC), Kyushu University, Japan.
[b] Center of Coevolutionary Research for Sustainable Communities (C²RSC), Kyushu University, Japan.
[c] International Institute for Carbon Neutral Energy Research (I²CNER), Kyushu University, Japan.
[d] Department of Materials Science and Engineering, Massachusetts Institute of Technology, USA.
[e] Helmholtz-Institute Münster (HIMS), IEK-12, Forschungszentrum Jülich, Germany
[f] Institute of Physical Chemistry, RWTH Aachen University, Germany
[g] JARA-HPC, Germany, Forschungszentrum Jülich & RWTH Aachen University, Germany
*harrington.frederick.george.302@m.kyushu-u.ac.jp
*s.grieshammer@fz-juelich.de
†Electronic Supplementary Information (ESI) available:. See DOI: 10.1039/x0xx00000x

the energy barrier at the saddle point between two oxygen sites, and consistently attribute strain dependence of the migration barrier to the steric hindrance and the bond strengths.[6,21,22] It is well established in bulk materials, however, that interactions between acceptors and vacancies also strongly influence transport due to the variation in the energy landscape, which alters the activation energy of conduction.[23–25] Referred to as defect interactions or defect association, this effect is clearly demonstrated in the series of RE-substituted CeO_2 (RE:CeO_2), where the lowest activation energies and highest conductivities are found for Gd- or Sm-substituted CeO_2 due to the beneficial balance between defect interaction and edge energies.[26] In contrast, smaller and larger rare-earth ions lead to higher activation energies and lower conductivities, due to strong defect interactions or increased barriers, respectively. Defect interactions are dependent on both elastic as well as electrostatic contributions, and in recent years, this has been more explicitly demonstrated using atomistic calculations.[27,28] Understanding the impact of defect interactions, as well as migration barriers, is crucial for strain engineering transport properties in solid state ionic conductors.

Experimentally, strain-modified ionic conductivity has primarily been studied in thin-film structures, however there is substantial scatter in the literature and very little consensus when comparing between different experimental results or when comparing experiments with simulations.[7,18,29] Studying strain-modified ionic transport in thin films can be challenging for two key reasons. First, as strain in such systems is typically engineered at interfaces via lattice mismatch, extremely thin layers are required to increase the volume fraction of strained material. Working with exceptionally thin layers leads to challenges in accurately measuring the strain state [30,31], as well as difficulties in accurately and reliably measuring the oxygen ion conductivity due to electrical leakage through the substrate[32] or sample holder,[33] or due to adsorbed protons.[34] Second, grain boundaries are often present in thin films and multilayers grown by physical vapour deposition. Grain boundaries can act to relax strain, are often heterogeneously distributed over the layer thickness,[35,36] and can dominate the transport properties.[37] In order to correlate changes in strain state to changes in conductivity, it is therefore imperative to either prevent grain boundaries or separate out their contribution to the total conductivity.

Further complications occur when it comes to making quantitative comparisons across the literature due to differences in measurement geometry. In prepared samples, such as films, lattice strain is rarely isotropic and instead biaxial strain is almost always observed. It has been well established computationally that for a biaxially strained system, the strain-modified conductivity will depend on the migration direction,[6,38] however this has not yet been demonstrated experimentally. Understanding the relation between migration in the in-plane and out-of-plane directions with respect to the strained axes is a crucial step towards achieving a deeper understanding of strain effects. In-plane measurements are typically more straightforward as these avoid issues with pinholes, do not require microelectrodes, and often result in impedance spectra that are easier to interpret. In contrast, out-of-plane measurements are more relevant for technological applications such as micro-SOFCs, memristors, and electrochemical actuators. In order to develop a relation between transport properties and transport direction, it is necessary to experimentally obtain the ionic conductivity for the in-plane and out-of-plane directions for the same system in terms of strain state and composition.

Recently, we demonstrated that in RE:CeO_2 the change in the activation energy with strain is sensitive to the size of the substitutional cations, such that a smaller substitutional, Yb, shows a significantly greater change in conductivity with strain than Gd, and a larger substitutional, La, showed less significant changes in conductivity.[39] Although the substitutional cations also affect the migration edge energies, empirical pair potential calculations demonstrated that the strain-dependence of these barriers could not explain the observed trend, suggesting that defect interactions and the correlated motion of ions must be taken into account to describe the difference in conductivity between the rare-earth substitutionals. The same trend for the change in activation energy with strain was also observed by Rushton et al. who performed molecular dynamic simulations on uniaxially strained RE:CeO_2 for each of the rare-earth substitutionals.[40] Deconvoluting the effects of strain on defect interactions and migration barriers is therefore vital for a full picture of how lattice strain affects ionic conductivity, and will pave the way for a more sophisticated rational-design approach to engineering ionic conductors.

In this study, we examine the interplay of migration barriers and defect interactions on the transport properties of biaxially strained CeO_2 by varying the size of the substitutional cations and the strain state. The substitutionals are La, Gd, and either Yb (experimentally) or Lu (computationally) which represent a size mismatch with the Ce host cations of 19.6%, 8.6%, and 1.5%/0.7% respectively (Figure 1a).[41] By growing on Nb-doped strontium titanate (Nb:STO) conductive single crystal substrates, epitaxial films could be fabricated allowing for out-of-plane conductivity measurements while avoiding any issues with grain boundaries. Rather than varying the thickness, we annealed the samples at different temperatures to relax the strain formed during growth, allowing the strain state to be systematically varied. Furthermore, the composition and strain state of these films are directly comparable to our previous study, grown on top of a $SrTiO_3$ buffer layer on insulating MgO substrates and measured in-plane. As such, by combining with our previous results we are able to experimentally separate the out-of-plane and in-plane transport properties of biaxially strained ceria.

Computational simulations are employed to deconvolute the effects of strain-modified migration barriers and defect interactions on the total conductivity. Migration barriers and defect interactions are calculated based on density functional theory for different substitutional cations and strain states. The energy parameters are applied in kinetic Monte Carlo (KMC) simulations to obtain the bulk ionic conductivity and activation energy, which is the result of the interplay of both the migration barriers and defect interactions. Strain effects on both migration barriers and defect association can be deliberately turned on and off, thus allowing the investigation of individual contributions to the change in ionic conductivity due to

strain. These findings not only provide new insights into the impact of strain on the conductivity of fluorite-structured oxygen-ion electrolytes, but should also give general guidance on the effects of strain on the anionic and cationic diffusion of a wide range of crystalline materials.

2 Theoretical considerations

In the unstrained cubic-CeO_2 $Fm\bar{3}m$ structure, oxygen transport takes place by jumps of oxygen ions into vacant sites along one of six equivalent <100> directions.[42] Along these pathways, a dumbbell of two Ce cations form a 'migration edge' which the oxygen ion must pass by overcoming the associated energy barrier, ΔE_{edge}. This is referred to as the Ce-Ce edge and is shown schematically in Figure 1b. The migration barrier is modified by the presence of either one or two rare-earth substitutionals in the migration edge, referred to as the Ce-RE edge and RE-RE edge, respectively.

Defect interactions between oxygen vacancies and substitutional cations (RE-v) as well as between multiple oxygen vacancies (v-v) can alter the initial and final state of the oxygen ion jump based on the local configuration of RE and v defects. This is termed 'configuration energy', ΔE_{conf}, and can be visualised as in Figure 1c. The migration energy, ΔE_{mig}, for a particular jump can be approximated taking into account both the edge energy and the configuration according to a linearized energy model[43] described by

$$E_{mig} = E_{edge} + \frac{\Delta E_{conf}}{2} \qquad (2)$$

In Equation (2), $\Delta E_{conf} = E_{conf,final} - \Delta E_{conf,initial}$, as shown in Figure 1c. This method has been successfully applied to the RE:CeO_2 system previously and has shown to be capable of replicating the transport properties in bulk materials.[26,28,42,44]

For biaxially strained CeO_2, the unit cell becomes distorted decreasing the bulk symmetry from cubic ($Fm\bar{3}m$) to tetragonal ($I4/mmm$). The in-plane strain (ε_{xx}=ε_{yy}) is defined as

$$\varepsilon_{xx} = \frac{a_{a/b} - a_0}{a_0} \qquad (3)$$

where $a_{a/b}$ is the strained a and b lattice parameters, and a_0 is the unstrained lattice parameter. For this system, there are four equivalent (orthogonal) in-plane migration directions, characterised by a migration edge energy, ΔE_{mig}^{in}, and two equivalent (anti-parallel) out-of-plane directions, characterised by ΔE_{mig}^{out}, as shown in Figure 1d with corresponding edge energies E_{edge}^{in} and E_{edge}^{out}.

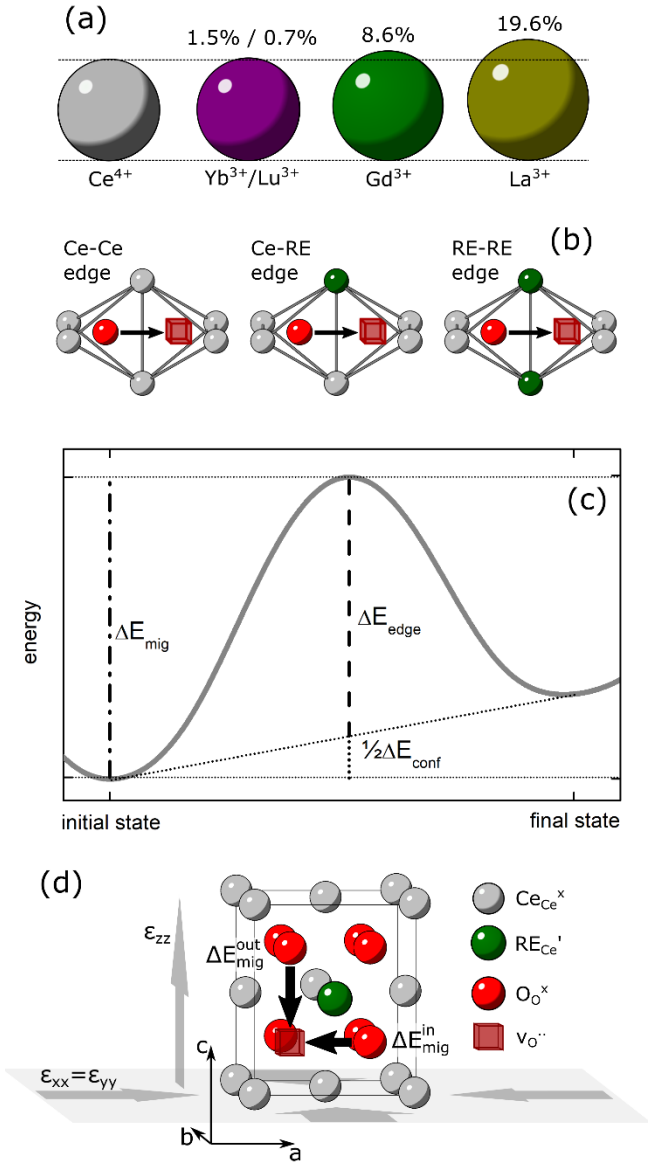

Figure 1 - (a) Ionic radii mismatch for the substitutional cations. (b) Possible configurations of migration edges in RE:CeO_2. (c) Migration energy for a given jump as a function of the edge and configurational contributions. (d) The distorted RE:CeO_2 unit cell under biaxially strain showing the in-plane and out-of-plane migration directions.

3 Methodology

3.1 Thin films fabrication

Thin films of 5 cat.% rare-earth substituted CeO_2 ($RE_{0.05}Ce_{0.95}O_{2-\delta}$; RE=La, Gd, Yb) were fabricated using pulsed laser deposition (PLD, AOV Co. Ltd., Japan) from the same ceramic targets as previously reported.[39] Details of the target synthesis is given in Ref. 39. Films were deposited on 10 × 10 mm (001) oriented 0.5 wt.% or 0.7 wt.% Nb-doped $SrTiO_3$ (Nb:STO; Shinkosha Co. Ltd., Japan or Dalian Keri Optoelectronic Technology Corp., China, respectively) with a thickness of either 200 nm or 80 nm, as calibrated by X-ray reflectivity. During deposition, the substrates were heated to 600 °C (according to the manufacturer's calibration) from behind using an IR lamp. To ensure effective heating, the substrates were either placed in contact with a Si disc or affixed to an Inconel disc using Ag paint. The oxygen partial pressure was held at 2.5 Pa, and the substrate and target were rotated continuously during deposition. A 248 nm KrF excimer laser (Lambda Physik COMPex 102) was used, operating at 2 Hz. The laser energy was set to 250 mJ, measured at 130 mJ outside the chamber, and focused to an area on the target of approximately 5 mm^2, corresponding to a fluence of 2.6 J cm^{-2}. After deposition the samples were cooled down over 1 h at the deposition pressure. The deposition parameters remained identical for all samples of the same thickness. After fabrication, the films were fractured into 4 approximately equal-size samples to be annealed at

varying temperatures to relax the strain that was present after deposition. One sample of each film was left 'as-grown' and the others were annealed in a box furnace at either 600 °C, 800 °C, or 1000 °C for 6 h with a 5 °C min^{-1} heating/cooling rate.

3.2 Structural Characterisation

The crystallographic orientation and lattice parameters of the samples, both out-of-plane and in-plane, were analysed using X-ray diffraction. A 5-circle diffractometer (Smartlab, Rigaku Corp., Japan) was used, equipped with a rotating Cu anode source and parallel beam optics via a Göbel mirror. High-resolution symmetric $2\theta/\omega$ scans and rocking curves were performed with a 2-bounce Ge(022) monochromator on the incident optics to assess the out-of-plane lattice parameters and orientation. Grazing incidence in-plane diffraction ($2\theta_\chi/\phi$ scans) was performed, without the monochromator and with an incident angle of $\omega = 0.4°$, to evaluate the in-plane lattice parameters and orientation. The reflections in the $2\theta/\omega$ and $2\theta_\chi/\phi$ scans were fitted using the pseudo-Voight function to assess peak position.

Transmission electron microscopy (TEM) was used to ensure no grain boundaries were present in the films and confirm their orientation. Cross-sections were prepared for TEM according to the 'lift-out' method using a dual-beam focused ion beam/scanning electron microscope (FIB/SEM, Helios Nanolab 600i, FEI Company, USA). Sections were taken out of the Gd:CeO_2 80 nm thick samples approximately near the centre, after electrical measurements had been performed. Thinning was performed at 30 keV, followed by 5 keV and 2 keV to prevent amorphous damage. A TEM equipped with aberration-corrector on both the probe-forming and imaging lens systems was used for analysis (JEM-ARM200F or JEM-ARM200CF, JEOL Ltd., Japan) operating at 200 keV. Electron energy loss spectroscopy (EELS) was performed in scanning TEM (STEM) mode using a Gatan Imaging Filter (GIF, Gatan Inc., USA) in dual-EELS mode, and X-ray energy dispersive spectroscopy (XEDS) was carried out using an SDD-type X-ray detector (solid angle of 2.0 sr).

3.3 Electrical measurements

The electrical conductivity of the samples was measured in the out-of-plane direction. Due to sub-micron-sized pinholes developing in the films during high-temperature annealing, it was decided that sputtering well-defined Pt electrodes onto the surface via photolithography should be avoided as it posed a risk of entering the pinholes and short circuiting the samples. Instead, Ag paste was hand painted on the RE:CeO_2 surfaces forming a number of approximately circular electrodes with a diameter of 0.5 – 1 mm. The back of the Nb:STO substrates were also painted in Ag paste such that a 2-probe electrical measurement could be performed between the film surface and the back of the substrate. The samples were subsequently annealed at 450 °C for 1 hr, with a 5 °C min^{-1} heating/cooling rate, to ensure good electrode contact, while avoiding higher temperature annealing which posed the risk of relaxing the strain present in the films. A calibrated optical microscope was used to image the electrodes used during the electrical measurements and a precise area of the electrode was calculated using the ImageJ software.

The samples were positioned in a custom-built sample holder, contacted from the back of the substrate using a Pt mesh, and on the surface electrode using a Pt needle. A tube furnace set on runners was then moved into position such that the sample was situated in the centre of the hot zone. This ensured the sample was symmetrically heated, avoiding any temperature gradients that may be present from the use of a hot stage,[45] and allowed the temperature to be accurately recorded from a thermocouple positioned adjacent to the sample. The measurements were carried out from 70 °C to 310 °C under static lab air, both heating and cooling to ensure reversibility, allowing the furnace to equilibrate for 1 h between each measurement.

Impedance spectroscopy was performed to assess the out-of-plane conductivity using a frequency response analyser (FRA, Alpha-A Frequency Analyser, Novocontrol Technologies GmbH & Co. KG, Germany or ModuLab XM MTS, Solartron Analytical, UK), applying an amplitude of 10 mV, zero DC bias, and measuring a frequency range of 1 MHz to 0.1 Hz**.** The resultant spectra were fitted using equivalent circuits with the Z-View software (Scribner, USA).

3.4 Density functional theory calculations

All density functional theory calculations were performed in the generalized-gradient approximation (GGA) with the exchange-correlation functional according to Perdew, Burke, and Ernzerhof (PBE)[46] using the VASP code.[47,48] The projector augmented wave (PAW) method[49] with an energy cutoff of 500 eV for plane waves was applied. Bulk calculations were performed in a 2×2×2 supercell with a 3×3×3 Monkhorst-Pack k-point mesh. Convergence criteria for ionic and electronic relaxation were set to 10^{-2} eV Å^{-1} and 10^{-4} eV, respectively. A Hubbard-U parameter was introduced for the 4f-orbitals of cerium with U_{eff}=5 eV in the simplified rotational invariant approach.[50]

Bulk lattice parameters were calculated in a range of -2% to +2% strain referenced to the bulk parameter of 5.49 Å in a and b direction. While the a and b parameter were fixed, the c parameter was varied, and results were fitted by Birch-Murnaghan equation of state to obtain the c parameter for a given strain state. Migration energies and interaction energies were calculated for -1%, 0%, and +1% strain in the a/b-plane in a 2×2×2 and 3×3×3 supercell with a 2×2×2 and 1×1×1 Monkhorst-Pack k-point mesh, respectively. Energies were extrapolated to infinite cell size to exclude finite size effects. The numbers of electrons were adapted for the respective defect charge and compensated by a homogeneous background charge. Calculations were performed for the dopants La, Gd, and Lu. Lu was chosen since DFT calculations with Yb showed serious convergence problems and the ionic radii of both elements are close. Interaction energies were computed by calculating the energies of defects with different separation distances. The climbing image nudged elastic band (CI-NEB) method with one interpolated image was used to calculate the migration edge energies.[51,52]

3.5 Kinetic Monte Carlo simulations

KMC simulations were conducted with the MOCASSIN software.[53] The migration energies of individual ion jumps were modelled from the DFT-derived edge energies and the difference of configuration energies in final and initial state according to Equation (2). The configuration energies were approximated by vacancy-vacancy and vacancy-dopant pair interactions as discussed in previous studies.[26,28,42,44]

Simulations were conducted for $Ce_{1-x}RE_xO_{2-x/2}$ with x = {0.05,0.1,0.15} in a temperature range of 450 K to 800 K with strain states of -1%, 0%, and +1%. 12×12×9 supercells of the I4/mmm unit cell with a total of 7776 ion positions were simulated. 250 to 5000 Monte Carlo steps per mobile particle were performed depending on the composition and temperature. The ionic conductivity was obtained from the displacement $\langle x \rangle$ of the oxygen ions in an external electric field E_x.

$$\sigma = q \cdot c \cdot \frac{\langle x \rangle}{E_x \cdot t} \qquad (4)$$

where q, c, and t are charge and concentration of the charge carriers and the simulated time, respectively. The field strength was chosen such that it had no influence on the ionic conductivity in accordance with previous studies.[26,28] For each data point the results of twelve simulations with different uniform, random cation distributions were averaged.

4 Results and discussion

4.1 Structure of biaxially strained thin films

Figure 2a shows the RE:CeO_2 004 and Nb:STO 003 reflections from out-of-plane XRD $2\theta/\omega$ scans performed on 200 nm thick samples. The full scans for all samples in this study are given in the supporting information (Figure S1), along with the rocking-curves taken about the RE:CeO_2 002 reflections (Figure S2), indicating high-quality oxide heteroepitaxial films with low mosaic spread. Grazing incidence in-plane $2\theta_\chi/\phi$ scans on the 200 nm thick samples are shown in Figure 2b. The XRD analysis reveals a single epitaxial relationship in the following orientation for all samples (based on the bulk cubic RE:CeO_2 $Fm\bar{3}m$ space group):

$$RE{:}\,CeO_2(001)||Nb{:}\,STO(001)$$

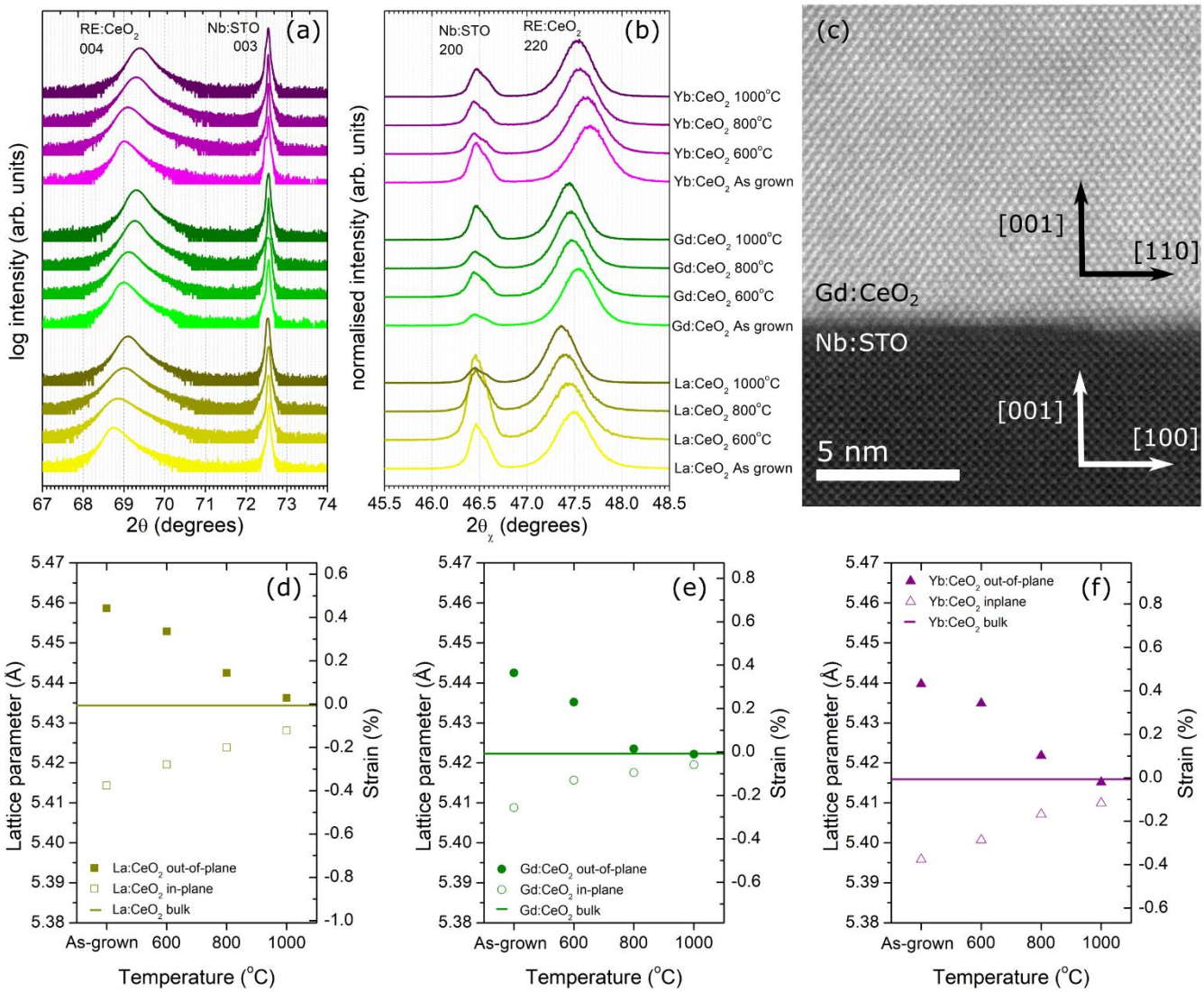

Figure 2 -(a) RE:CeO_2 004 and Nb:STO 003 reflections from out-of-plane XRD $2\theta/\omega$ scans for 200 nm thick samples. (b) Grazing incidence in-plane $2\theta_\chi/\phi$ scans for 200nm thick samples. (c) Typical HAADF-STEM image. Lattice parameters for (d) La:CeO_2 (e), Gd:CeO_2 and (f) Yb:CeO_2 200 nm thick samples.

$$RE{:}CeO_2[110]||Nb{:}STO[100]$$

Grain boundaries are known to result in changes in the total conductivity and activation energy of oxygen ion conducting films, preventing the reliable identification of strain-modified conductivity.[36,54] To ensure no grain boundaries were present in the films, we observed the microstructure using TEM imaging. A representative high-angle annular dark-field scanning transmission electron microscopy (HAADF-STEM) image is shown in Figure 2c, confirming the epitaxial relationships and indicating that the films are free from grain boundaries. Further TEM images and elemental analyses are given in Figure S5 and Figure S6 in the supporting information.

From Figure 2a and Figure 2b, clear shifts in the RE:CeO_2 004 out-of-plane reflections and 220 in-plane reflections, respectively, are observed as the annealing temperature is increased. With increasing temperature, the out-of-plane reflections shift to higher 2θ angles, and therefore a decreasing lattice spacing, while the in-plane reflections shift to lower $2\theta_\chi$ angles, signifying increasing lattice spacing. The in-plane and out-of-plane lattice parameters are given for 200 nm thick La:CeO_2 (Figure 2d), Gd:CeO_2 (Figure 2e), and Yb:CeO_2 (Figure 2f) films as a function of annealing temperature along with the bulk lattice parameters measured in the bulk parent material. As grown, there is a clear in-plane compressive strain, up to about -0.4%, and out-of-plane expansion, up to about 0.5%, which relaxes close to the bulk values as the samples are annealed at higher temperatures.

Such behaviour is characteristic of an in-plane biaxial compression and out-of-plane Poisson dilation, thereby decreasing the bulk symmetry from cubic ($Fm\bar{3}m$) to tetragonal ($I4/mmm$). The Poisson ratio, ν, was observed to be in the range of 0.34 to 0.36. This is comparable to our previous work on RE:CeO_2 films grown in near-identical conditions,[39] where the strain is assumed to be due to growth processes during physical vapor deposition,[55,56] rather than lattice or thermal mismatch with the substrate. The findings here support this assumption as the films are relatively thick (200 nm), and therefore interface mismatch should be localised to a small volume fraction of the samples and not represent the average lattice parameters, and both the lattice and thermal expansion coefficient mismatch between RE:CeO_2 and Nb:STO would lead to an in-plane tensile strain,[57,58] which is clearly not observed. Therefore, by annealing the samples at different temperatures, the lattice strain present in the films can be systematically tailored without resorting to changing the film thickness or substrate.

4.2 Out-of-plane transport in biaxially strained thin films

Typical Nyquist plots of the impedance spectra are given in Figure S7 in the supporting information, from which the ionic conductivity can be extracted from a high-frequency arc as previously reported for substituted-ceria films grown on Nb:STO substrates and measured in a similar geometry.[59,60] The out-of-plane conductivities of the 200 nm thick samples are plotted as a function of reciprocal temperature in Figure 3. The bulk (grain core) conductivity of the parent materials used to grow the films, as previously reported,[39] is shown for comparison. The conductivity of all samples can be fitted according to Equation 1, with a single activation energy as listed in Figure 3. As the amount of biaxial compressive strain increases in the samples, the conductivity decreases, and the activation energy increases compared to bulk behaviour. Such behaviour is expected from compressive strain, as predicted from previous computational studies.[6,22,38] From Figure 3, the most significant changes in conductivity are observed for Yb:CeO_2 which decrease by about over 2 order of magnitude at 150°C, followed by Gd:CeO_2 which decreased by over 1 order of magnitude, and then La:CeO_2, where the trend becomes harder to observe. These trends are consistent for both the 200 nm and 80 nm thick films, as shown in the supporting information.

Activation energies and pre-exponential factors extracted from fitting Equation (1) to the data in Figure 3 (and 80 nm thick films as shown in Figure S8) are plotted in Figure 4 as a function of in-plane strain. The change in activation energy with lattice strain is clear, with in-plane compressive strain leading to increases in the activation energy for all substitutional species. As with the conductivity, the most significant increase in activation energy is for Yb:CeO_2, followed by Gd:CeO_2, and then La:CeO_2. We leave the discussion for the reasons behind these observations for Section 4.6.

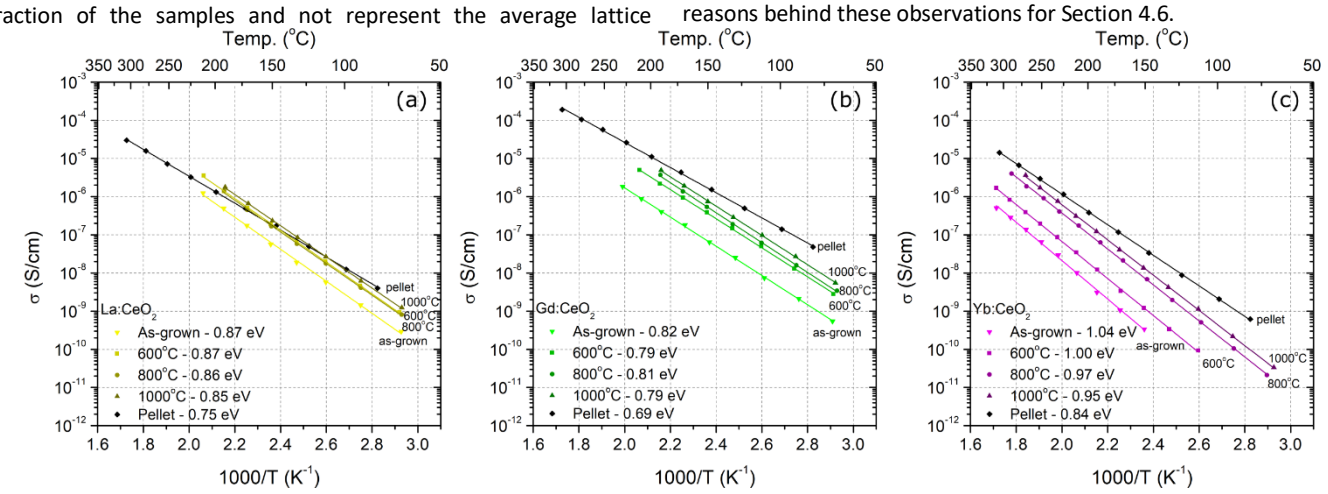

Figure 3 - Ionic conductivity of (a) La:CeO_2 (b), Gd:CeO_2 and (c) Yb:CeO_2 films for strain states corresponding to various annealing temperatures. The data for the parent pellets, as previously reported,[39] is plotted for comparison

Although the conductivity and activation energy approach bulk behaviour as the annealing temperature is increased and the strain is relaxed, there is still a difference between the 'relaxed' thin film samples and the bulk pellets. In addition, there is also a general trend of the pre-exponential factor rising as the annealing temperature increases, as seen in Figure 4b. As previously discussed, changes in the lattice strain state should not yield any substantial changes in the terms contributing to the pre-exponential factor. As such, the difference in conductivity and activation energy between the bulk pellets and 'relaxed' films as well as the increasing pre-exponential factors after annealing may suggest a secondary effect is taking place during annealing which impacts the transport properties. One possibility which might explain an increase in the pre-exponential factors, would be a change in the charge carrier concentration during annealing, perhaps due to the as-grown films exhibiting a high degree of oxygen deficiency. This, however, is unlikely, as the samples should approach bulk non-stoichiometry with higher annealing temperatures and the pre-exponential factors of these samples should therefore be in agreement with the pellet. Furthermore, significantly reduced substituted-ceria should display a higher conductivity compared to the pellet due to the increased oxygen vacancy concentration and introduction of n-type conductivity,[61] which is not observed.

A more likely explanation may be segregation of rare-earth cations to the surface of the films, creating a layer with a much higher rare-earth concentration. In bulk substituted-ceria, as the substitutional concentration increases above ~10 cat.%, the conductivity decreases, the activation energy increases, and the pre-exponential increases.[24,62] Therefore, a highly enriched layer at the surface may contribute to the resistance of the film when measured in the out-of-plane geometry. Surface segregation has previously been reported for Gd-substituted ceria films grown by PLD, where the width and concentration of the enriched layer were shown to increase with annealing from 600 °C to 1000 °C, and could be as high as a site fraction of 40 %.[11] To check this hypothesis, the out-of-plane conductivity of a hypothetical 200 nm thick 5 cat.% Gd:CeO_2 film with a 5 nm segregation region with a 20 cat.% Gd concentration was calculated based on bulk conductivity values from the literature [62] and plotted in Figure S9 of the supporting information. Although this is a simplified model of a segregation layer, and the thickness and substitutional concentration may be different in the films, it can be shown that both the increase in activation energy and pre-exponential factor can be replicated (Table S2), and that the total conductivity is even in reasonable agreement with the 'relaxed' Gd:CeO_2 sample measured. Indeed from EELS analysis carried out in the TEM (Figure S6), an enrichment of Gd is observed at the surface of a Gd:CeO_2 film annealed at 1000 °C. The role of a segregation layer on the measured conductivity is further supported by comparing to our previous work, where the conductivity of films annealed under the same conditions was measured in-plane, and the 'relaxed' films showed a much better agreement with bulk behaviour and did not display an increase in the pre-exponential factor.[39] In this case the segregation layer would be a parallel path, and therefore have a much less significant impact on the transport properties. While such segregation effects may take place during annealing, these would have the opposite effect on the overall conductivity and activation energy compared to relaxing the compressive lattice strain. Therefore, these should be considered a secondary effect, and the significant changes in the conductivity observed with annealing are still consistent with behaviour dominated by lattice-strain effects.

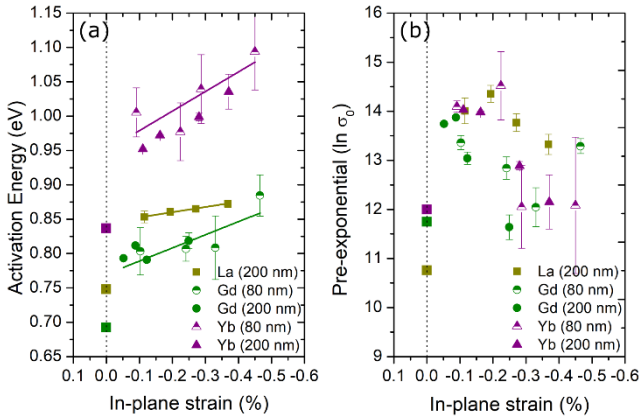

Figure 4 - (a) Activation energies and (b) pre-exponential factors of the conductivity of thin films depending on strain state. The larger square symbols represent values taken from the bulk parent material.

4.3 Defect-interactions and edge energies from DFT calculations

For biaxial strain between -2% to +2%, a linear relationship is observed between the in-plane, a, b, parameters and the out-of-plane c parameter as described by a Poisson relation, shown in Figure S10 in the supporting information. Consequently, a linear relation between the volume and the strain can be observed (Figure S10). The Poisson ratio, ν, is calculated to be 0.23, which is consistent with previous empirical pair potential results,[6,63] although smaller than previously reported experimental results in the range of 0.29-0.31,[64,65] or the 0.34-0.36 range found experimentally in this study.

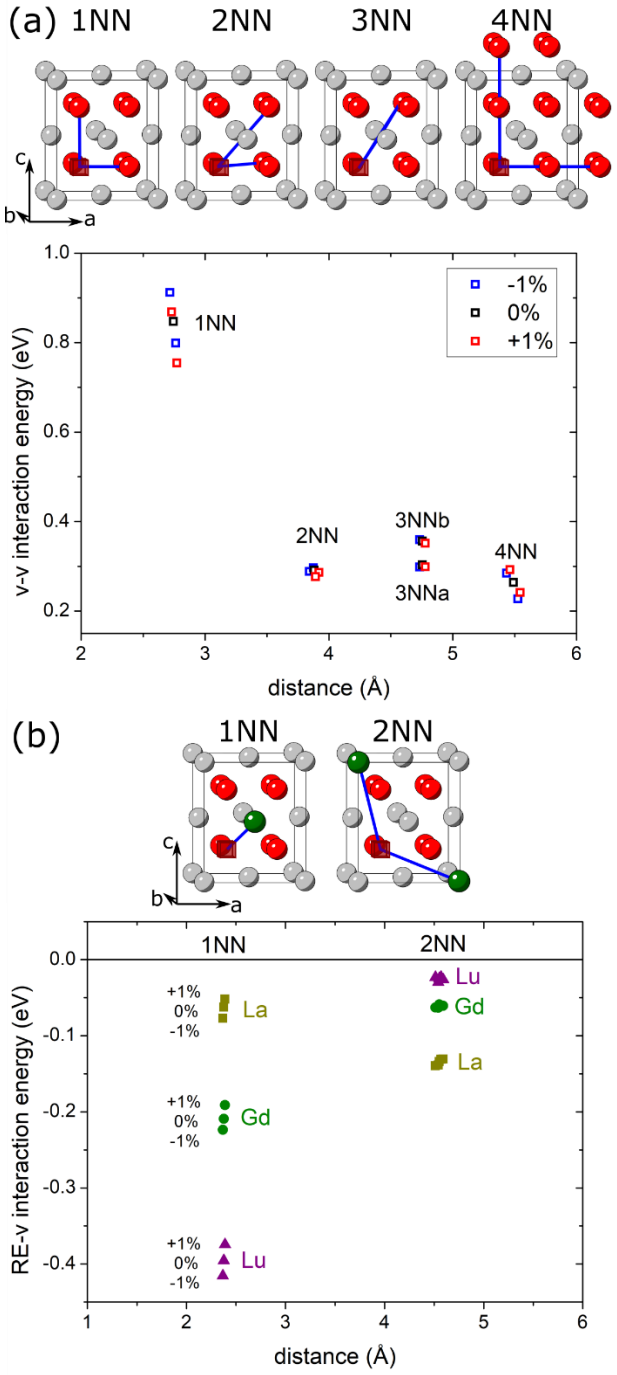

Figure 5 - DFT calculated defect-interactions between (a) two oxygen vacancies and (b) a substitutional rare earth ion and an oxygen vacancy for different strain states, rare earth cations, and distances.

Vacancy-vacancy interaction energies were calculated up to the fifth nearest-neighbour (5NN) position and evaluated relative to this position, as shown in Figure 5a. Due to the change in symmetry from cubic to tetragonal under biaxial strain, there are two distinct interaction vectors for the 1NN, 2NN, and 4NN position, while it does not affect the 3NN vectors. However, for the 3NN interactions there are two distinct positions already in the unstrained case, distinguished by the presence or absence of a cation positioned along the interaction vector. There is essentially no dependence on strain for the 2NN and 3NN interaction energies as the increase (decrease) in the a, b parameters are compensated for by a decrease (increase) in the c parameter. For the 1NN and 4NN interactions, however, there is a clear change with strain state. These interaction vectors are parallel to the a, b parameters or the c parameter, and therefore either are parallel or perpendicular to the biaxial strain plane. The relation between vacancy-vacancy interaction energies and strain for the 1NN and 4NN interactions can be well described by a linear function for each interaction type, given in Table S3 in the supporting information. It should be noted that the change is much stronger than suggested by a purely Coulombic interaction, and consequently, elastic interactions must play a determining role.

Interactions between the oxygen vacancies and rare-earth cations (La, Gd, or Lu) were calculated up to the 3NN position. The 1NN and 2NN interaction energies are shown in Figure 5b relative to the 3NN position, which was set to zero. The smaller substitutional (Lu) shows a stronger 1NN interaction, but a weaker 2NN interaction, while the trend is reversed for the larger substitutional (La), which is consistent with findings from previous studies.[28] The 1NN interaction is along

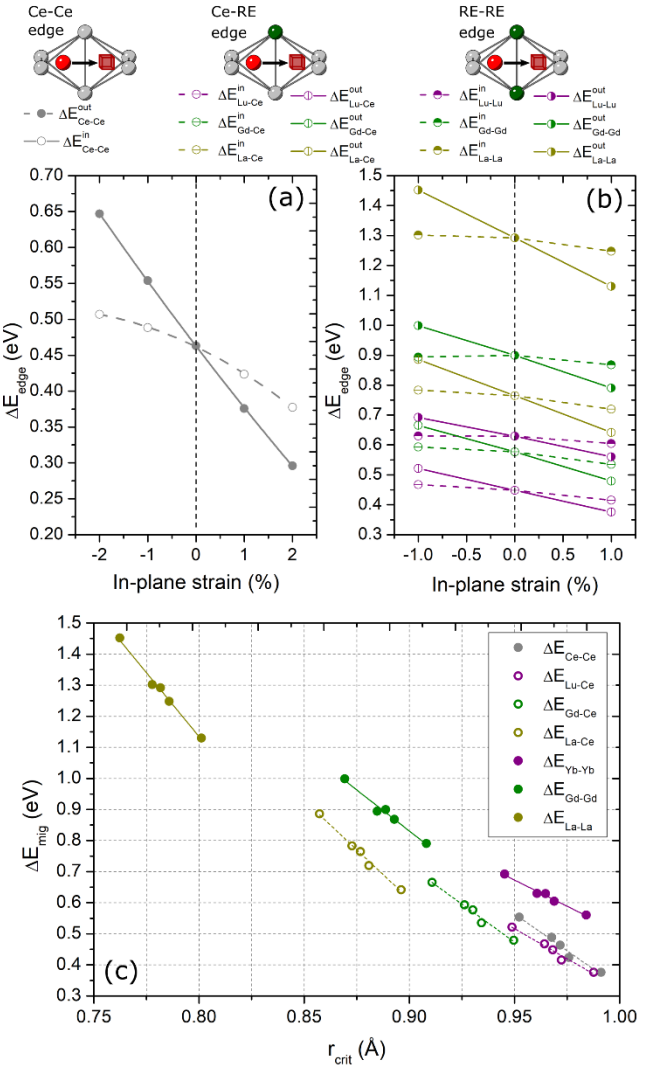

Figure 6 - (a) Edge energy of Ce-Ce edge depending on strain state, and (b) edge energy of all Ce-RE and RE-RE edges depending on strain state calculated by DFT. (c) Relation between edge energies and the critical radius.

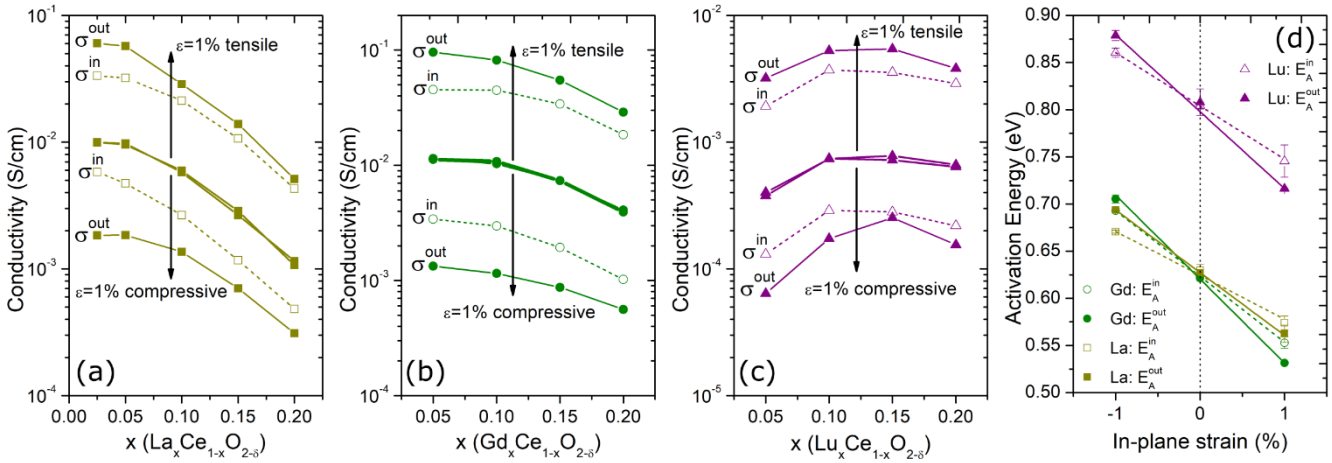

Figure 7 - Simulated conductivity using the KMC method at 227°C (500K) for different strain states as a function of dopant fraction for (a) Lu:CeO_2, (b) Gd:CeO_2, and (c) La:CeO_2. (d) The resulting activation energy for x=0.05. Lines are guide to the eye.

the body diagonals and therefore shows no directional dependence as the symmetry of the cell is reduced under strain. There are two distinct 2NN interactions for the strained case, however the effect of strain on the interaction energies is so small that these changes can be considered negligible. For the 1NN interaction, the strength clearly increases for compressive strain, and decreases for tensile strain. As with the vacancy-vacancy interactions the relationship between interaction energy and strain can be described by a linear function (Table S4 in the supporting information), and again, the strain-dependence is much more significant than can be inferred from Coulomb interactions alone.

The effect of biaxial strain on the in-plane, ΔE_{Ce-Ce}^{in}, and out-of-plane, ΔE_{Ce-Ce}^{out}, barriers of the Ce-Ce edge is shown in Figure 6a. The change in migration edge energy is more pronounced for the out-of-plane direction than the in-plane direction. The out-of-plane energies follow a linear trend, while the in-plane energies follow a parabolic dependence, consistent with previous computational reports.[6,38] The presence of either one or two rare-earth substitutionals in the migration edge, referred to as the Ce-RE edge and RE-RE edge respectively, modifies the migration barrier and the change with biaxial strain is shown in Figure 6b for both the in-plane and out-of-plane directions. All edges show similar dependences as the Ce-Ce edge and can be expressed by linear functions for the out-of-plane direction, and parabolic dependence for the in-plane direction (as detailed in Table S5 and Table S6 in the supporting information). Comparing the changes in edge energy for the same direction (in-plane or out-of-plane) and type (RE-Ce or RE-RE) consistently yields a larger effect with strain for the larger La substitutional, followed by Gd and then Lu.

In general, the edge energy increases for larger dopant ions on the edge and for decreasing distance of the ions due to strain. This is in accordance with the critical radius model which describes the radius of a sphere that can just pass through the edge configuration in the transition state.[19] From geometrical reasons the critical radius r_{crit} in the ceria structure is defined as:

$$r_{\mathrm{crit}} = \frac{d_{AB} - r_A - r_B}{2} \qquad (5)$$

where d_{AB} is the distance between sites based on the lattice parameter, and r_A and r_B are the ionic radii of the species at the edge. The dependence of edge energies on r_{crit} is illustrated in Figure 6c and a monotonic increase is observed for decreasing values of r_{crit}. It is apparent that the energies for the RE-RE edge are higher than for the RE-Ce edges at the same r_{crit}. This could be explained by reasons of symmetry; for RE-RE edges the oxygen ion at the transition state is limited by dopant ions on both sides while it has the Ce-ion on one side in the case of the RE-Ce edge resulting in a more favourable, curved migration path. The figure also shows that the slope of the energy curve gets slightly steeper for smaller r_{crit} as the interaction of the oxygen ion with the edge cations in the transition state gets increasingly unfavourable.

4.4 Conductivity and activation energy from Kinetic Monte Carlo simulations

Kinetic Monte Carlo simulations were applied to assess the total conductivity and activation energy using the strain dependence of the vacancy-vacancy interactions, interactions between rare earth cations and oxygen vacancies, and migration edge energies, as calculated by DFT. The conductivity at 227 °C (500 K) as a function of substitutional fraction is shown in Figure 7 for La:CeO_2, Gd:CeO_2, and Lu:CeO_2. Each show a broad maximum in conductivity as a function of substitutional fraction. This behaviour is in agreement with experimental results,[23,24,66] and underlines the ability of the KMC simulations to capture transport behaviour of these systems. For all substitutionals, tensile strain leads to an increase of the conductivity, and compressive strain leads to a decrease. These changes in the conductivity are clearly more significant for the out-of-plane direction than for the in-plane direction.

The activation energy between 177 and 527 °C (450 – 800 K) as function of strain for 5 cat.% RE:CeO_2 is given in Figure 7d. The activation energy of Lu:CeO_2 is significantly higher than of La:CeO_2 or Gd:CeO_2, which corresponds to the lower conductivity, and is also consistent with experimental findings. The influence of strain on the activation energy is similar for Lu:CeO_2 and Gd:CeO_2, but smaller for La:CeO_2.

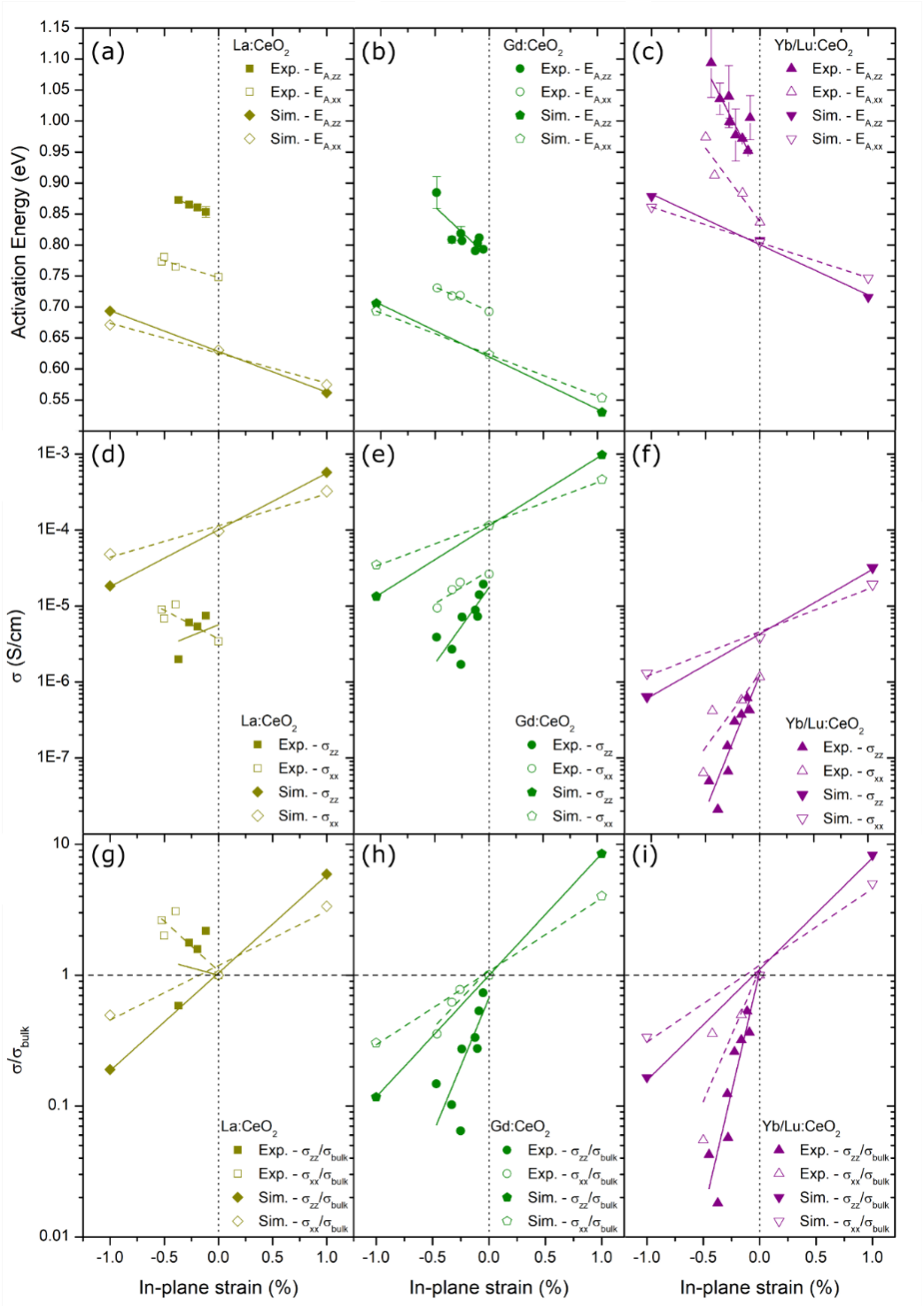

Figure 8 - Experimental and simulated results for (a)-(c) activation energy, (d)-(f) ionic conductivity at 227 °C (500 K) and (g)-(i) the relative conductivity at 227 °C (500 K) with respect to the unstrained value. The experimental in-plane transport properties are taken from ref.[39] Lines are guide to the eye.

4.5 Effect of migration direction

Figure 8 shows the strain dependence of the activation energy, conductivity, and the relative change in conductivity for both the in-plane and out-of-plane directions according to our experimental measurements and KMC simulations. The in-plane transport properties are taken from our previous study on the same RE:CeO_2 compositions, same film orientation, and similar range in strain values.[39] Consistently, the change in the activation energy and conductivity is more significant in the out-of-plane direction compared to in-plane, from both the experimental and computational data. Experimentally, the trend is most clearly observed for Gd:CeO_2 where at ~0.5% strain the difference between the out-of-plane and in-plane activation energy is more than 0.1 eV and the difference in conductivity is approximately a factor of 10.

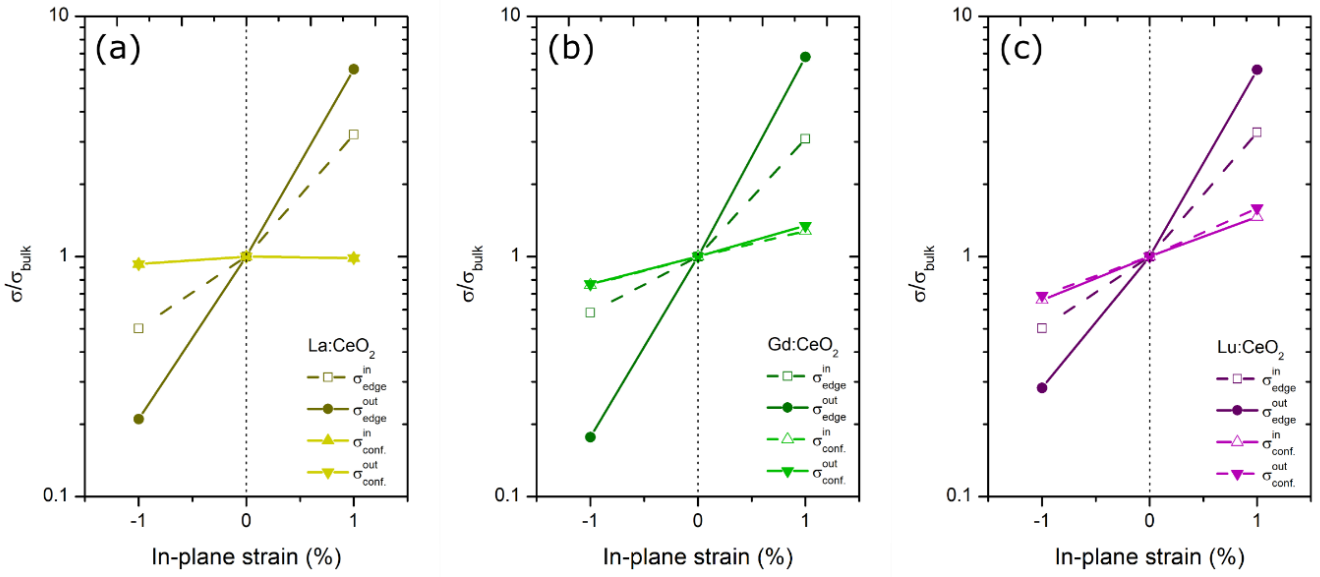

Figure 9 - Relative change of the in-plane and out-of-plane conductivity with strain from KMC simulations at 500K, by varying either the edge barriers or the defect-interactions while keeping the other constant.

These differences can be best explained from the changes in the edge energies calculated from DFT. The energy barriers for the Ce-Ce, RE-Ce, and RE-RE all show directional dependence as illustrated in Figure 6a and Figure 6b. As demonstrated in Figure 6c, the edge energies are well described by a linear dependence on the distance between the two cations for the same pair of cationic species. For the out-of-plane edges, ΔE^{out}, the oxygen ion must hop between two cations which are aligned within the strain plane, and therefore the change in distance between the cations is directly described by the magnitude of the biaxial strain. For the in-plane edges, ΔE^{in}, the vector between the two cations is neither parallel nor perpendicular to the strain plane, and therefore changes by a lesser extent. In contrast, the defect interactions are not expected to yield a directional anisotropy. The RE-v interactions show no directional dependence (Figure 5b) as the interactions lie along the body diagonals, which are neither parallel nor perpendicular to the strain plane. The v-v interactions do show a directional dependence for the 1NN and 4NN distances (Figure 5a), but there is no large difference between the energy barrier for vacancies jumping away from one another along the in-plane or out-of-plane direction.

Comparing between the experimental and simulated values for Gd:CeO_2, the unstrained, bulk activation energies are within 0.1 eV and the conductivity within an order of magnitude. Deviations between experimental values and simulated are expected as the DFT-derived energies are not exact, the energy model is limited and the pre-exponential factor is approximated by a typical value of 10^{13} Hz. In addition, differences might arise from the comparison of the simulated bulk and measured thin films due to inhomogeneous strain or cation segregation as discussed above. Nevertheless, the slopes representing the strain dependence of the activation energy and conductivity from experiment and simulation are in good agreement. The most distinct difference is observed for Yb:CeO_2/Lu:CeO_2 as experimental values show a stronger dependence on the strain state. This might be due to the difference between Yb and Lu despite their similar ionic radii. In addition, clustering of dopant ions has an influence on the ionic conductivity as well[28] which could be important especially for small dopants with strong defect association such as Lu and Yb.

4.6 Effect of rare-earth ionic radii

Experimental measurements of biaxially strained films in Figure 8 consistently show for both migration directions that the strain-dependence of the transport properties in RE:CeO_2 are significantly dependent on the size of the substitutional cations. The smaller acceptor, Yb, yields much larger changes in the conductivity and activation energy than Gd, while for the larger acceptor, La, the changes in conductivity are negligible. To investigate these effects, we carried out KMC simulations varying just the edge energies or just the defect interactions while keeping the other fixed as in the non-strained state. The relative changes in the conductivities are shown in Figure 9. It is clear from the data that the anisotropic directional dependence of the conductivity is only observed when the edge energies are varied with strain, while the configurational energies lead to no differences between the in-plane and out-of-plane transport. This supports our previous assumption that the differences in the edge barriers, as calculated from DFT, are the origin of the directional anisotropy.

The change of the ionic conductivity due to changes of the edge barriers is in reasonable agreement across each of the substitutional species. Initially, this is surprising, as it was previously shown in Figure 6b that the change in the RE-Ce and RE-RE barriers being more sensitive to strain for the larger cation La and less so for the smaller cation Lu. To understand why the differences in the strain dependence of the edge barriers for the three acceptor cations do not appear to substantially influence the resultant conductivity, it is important to discern how each type of barrier contributes to long-range oxygen ion motion. Figure 10 shows the fraction of attempted

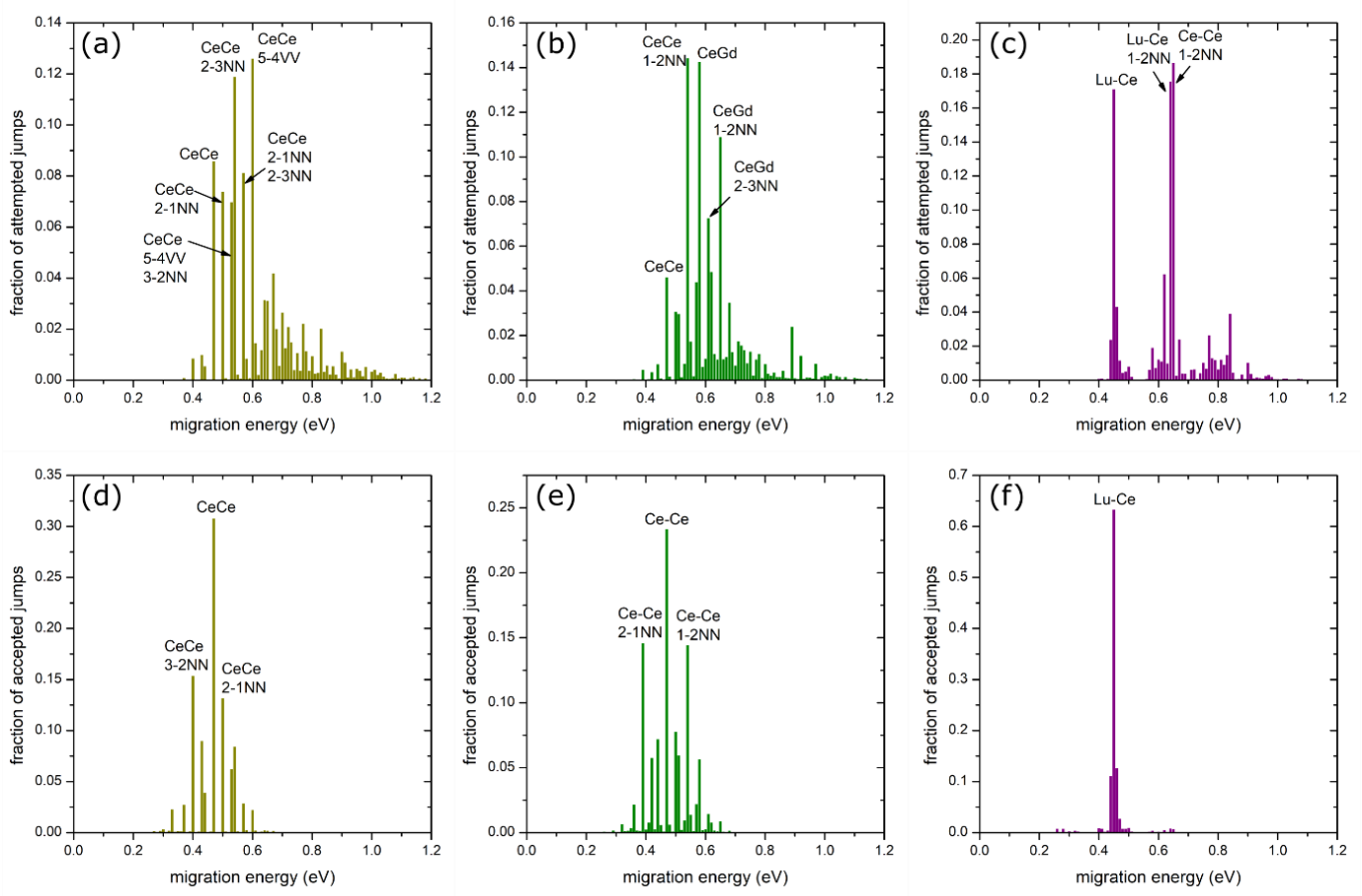

Figure 10 - Fraction of attempted (a, b, c) and successful (d, e, f) in-plane jumps for La (a, d), Gd (b, e), and Lu (c, f) from KMC simulations.

and successful in-plane jumps for vacancies in RE:CeO_2 for each substitutional species simulated using KMC. For Gd:CeO_2 the distribution of jump attempts is broad, including jumps across the Ce-Ce edge, the Ce-Gd edge, and jumps involving movement to and from the substitutional. The same is true for successful jumps, mainly dominated by jumps without configurational influence and jumps between the 1NN and 2NN position of the substitutional. Conversely, for La:CeO_2, Ce-Ce edges dominate the attempted and successful jumps, where jumps through the Ce-La edges are in a minority as vacancies are most stable in the 2NN position. Hence, despite the Ce-La and La-La edges (>0.6 eV) being significantly modified by strain, these have a minimal impact on the long-range ionic motion. For Lu:CeO_2 attempts are dominated by jumps across the Lu-Ce edge and from the 1NN position of Lu to the 2NN position. Due to the strong trapping the attempts away from the dopant are mostly unsuccessful and consequently successful jumps are dominated by jumps around the Lu dopant that do not contribute to the long-range transport. While the presence of lattice strain does modify the barriers present, the distribution of the histograms is similar for all strain states, as shown in Figure S11 in the supporting information.

Looking at the strain-dependence of the conductivity in Figure 9, when only the defect-interaction is varied, reveals that for La:CeO_2, ΔE_{conf} has a negligible influence on the conductivity while the effects are more significant for Gd:CeO_2, and even more so for Lu:CeO_2. This demonstrates that for smaller substitutionals, where the RE-v interactions are stronger, the strain dependence of the defect-defect interactions plays a larger role in the strain-dependence of the transport properties. However, comparing the impact of strain on the conductivity due to edge energies and defect interactions suggest that the change in edge energies is the most significant cause of the change in transport properties with strain. This can be explained by the fact that all the edge energies are modified, including the Ce-Ce edge which is crucial for long-range ionic transport, while the defect interactions only effect the barriers in the vicinity of substitutionals which do not always significantly contribute to the conductivity (Figure 10). The effect of defect interactions is largest for Lu:CeO_2, as the jumps away from Lu play a crucial role in long-range transport due to the strong trapping between Lu and vacancies.

It should also be noted, however, that there is a discrepancy between relative changes in the conductivity with strain between the simulations and experimental results, as shown in Figure 8g-I. For the smaller substitutionals, Yb/Lu, the simulations predict a significantly smaller change in the conductivity than overserved experimentally and do not show the conductivity of Lu:CeO_2 to be more sensitive to strain than Gd:CeO_2 as is observed experimentally for Yb:CeO_2. At this point it is not entirely clear as to the reason for these discrepancies. Experimentally, it could be caused by surface segregation, as previously discussed, inhomogeneities in the strain state, clustering of the acceptor substitutionals, differences between

Yb and Lu, or due to interactions or mechanisms not fully captured in the simulations. Nevertheless, these results shows that understanding the role of the ionic radii of substitutionals is vital for engineering strain-modified transport in RE:CeO_2. Furthermore, a full description of the effect of strain on oxygen migration in RE:CeO_2 and other solid state electrolytes must take into account the variation in migration barriers, defect interactions, and distribution of hopping events on long-range transport.

5 Conclusions

We measured the out-of-plane conductivity in biaxially strained epitaxial thin films of ceria substituted with La, Gd, and Yb. A gradual variation of the in-plane compressive strain was possible by annealing at various temperatures, while avoiding any complications due to grain boundaries. We have experimentally demonstrated that the change in conductivity and activation energy due to a biaxial strain is more significant for the out-of-plane direction than for the in-plane, confirming what had previously been predicted computationally. Furthermore, it was shown that the size of the substitutional cations plays a significant role on the strain dependence of the transport properties. The largest change in conductivity, of approximately two orders of magnitude at around 150 °C, is observed for the smallest dopant Yb followed by Gd and then La.

Bulk ionic conductivity for different dopants and strain states was simulated with the Kinetic Monte Carlo method based on DFT derived energy parameters. This approach meant that variations in the migration edge barriers and defect interactions could be correlated with the long-range motion of vacancies. We have shown that even though a subset of high-energy migration barriers is observed to vary the most with strain, these do not significantly contribute to the long-range conductivity. By decomposing the contributions from migration edge energies and defect-interactions, we have observed that both contribute to the strain-modified conductivity, however the change due to variations in migration edge energies is much more substantial than changes due to defect interactions.

In summary, it is important to understand how the ionic transport properties of functional oxides are impacted by lattice strain. Lattice strain may occur, unintentionally, during device fabrication or operation, or may be deliberately engineered for enhanced functional properties. A full description of the strain-dependent transport must take into account both migration edge energies and defect interactions, as well as their impact on long-range ionic motion. By considerations of the size of substitutional cations, substitutional concentration, and migration direction, it may be possible to realize even more significant enhancements in ionic transport through lattice strain.

Conflicts of interest

There are no conflicts to declare.

Acknowledgements

S.G. gratefully acknowledges the computing time granted by the JARA Vergabegremium and provided on the JARA Partition part of the supercomputer CLAIX at RWTH Aachen University. G.F.H. gratefully acknowledges financial support from a Kakenhi Grant-in-Aid for Encouragement of Young Scientists (B) Award (No. JP18K13992), and the Platform of Inter/Transdisciplinary Energy Research Support Program (Q-pit) at Kyushu University. G.F.H., H.L.T., and K.S. are also grateful for support from the Progress 100 program of Kyushu University, and the International Institute for Carbon-Neutral Energy Research (WPI-I2CNER), both supported by MEXT, Japan, and the Center of Innovation Science and Technology based Radical Innovation and Entrepreneurship Program (COI Program), by the Japan Science and Technology Agency (JST) (grant number: JPMJCE1318). H.L.T acknowledges support for his research from the Department of Energy, Basic Energy Sciences under award number DE-SC0002633 (Chemomechanics of Far-From-Equilibrium Interfaces).

References

1 C. Zhao, Y. Li, W. Zhang, Y. Zheng, X. Lou, B. Yu, J. Chen, Y. Chen, M. Liu and J. Wang, *Energy Environ. Sci.*, 2020, **13**, 53–85.

2 S. Schweiger, R. Pfenninger, W. J. Bowman, U. Aschauer and J. L. M. Rupp, , DOI:10.1002/adma.201605049.

3 C. Balaji Gopal, M. García-Melchor, S. C. Lee, Y. Shi, A. Shavorskiy, M. Monti, Z. Guan, R. Sinclair, H. Bluhm, A. Vojvodic and W. C. Chueh, *Nat. Commun.*, 2017, **8**, 15360.

4 N. Muralidharan, C. N. Brock, A. P. Cohn, D. Schauben, R. E. Carter, L. Oakes, D. G. Walker and C. L. Pint, *ACS Nano*, 2017, **11**, 6243–6251.

5 X. Wen, W. Yang, Y. Ding, S. Niu and Z. L. Wang, *Nano Res.*, 2014, **7**, 180–189.

6 R. A. De Souza, A. Ramadan and S. Hörner, *Energy Environ. Sci.*, 2012, **5**, 5445–5453.

7 C. Korte, J. Keppner, A. Peters, N. Schichtel, H. Aydin and J. Janek, *Phys. Chem. Chem. Phys.*, 2014, **16**, 24575–24591.

8 A. Fluri, D. Pergolesi, V. Roddatis, A. Wokaun and T. Lippert, *Nat. Commun.*, 2016, **7**, 10692.

9 M. Kubicek, Z. Cai, W. Ma, B. Yildiz, H. Hutter and J. Fleig, *ACS Nano*, 2013, **7**, 3276–3286.

10 Y. P. Ivanov, M. Kubicek, M. Siebenhofer, A. Viernstein, H. Hutter, J. Fleig, A. Chuvilin and Z. Zhang, *Commun. Mater.*, 2020, **1**, 2–9.

11 G. F. Harrington, S. J. Skinner and J. A. Kilner, *J. Am. Ceram. Soc.*, 2018, **101**, 1310–1322.

12 B. Koo, H. Kwon, Y. Kim, H. G. Seo, J. W. Han and W. Jung, *Energy Environ. Sci.*, 2017, 1–20.

13 A. Kushima, S. Yip and B. Yildiz, *Phys. Rev. B - Condens. Matter Mater. Phys.*, 2010, **82**, 1–6.

14 A. Herklotz, D. Lee, E. Guo, T. L. Meyer, J. R. Petrie and H. N. Lee, *J. Phys. Condens. Matter*, 2017, **29**, 493001.

15 V. Esposito and I. E. Castelli, *Adv. Mater. Interfaces*, 2020, **7**, 1–22.

16 X. Guo and J. Maier, *Adv. Mater.*, 2009, **21**, 2619–2631.
17 X. Guo, *Scr. Mater.*, 2011, **65**, 96–101.
18 K. Wen, W. Lv and W. He, *J. Mater. Chem. A*, 2015, **3**, 20031–20050.
19 J. Kilner and R. Brook, *Solid State Ionics*, 1982, **6**, 237–252.
20 C. Korte, N. Schichtel, D. Hesse and J. Janek, *Monatshefte fur Chemie*, 2009, **140**, 1069–1080.
21 A. Kushima and B. Yildiz, *J. Mater. Chem.*, 2010, **20**, 4809–4819.
22 M. Alaydrus, M. Sakaue, S. M. Aspera, T. D. K. Wungu, N. H. Linh, T. P. T. Linh, H. Kasai, T. Ishihara and T. Mohri, *J. Phys. Soc. Japan*, , DOI:10.7566/JPSJ.83.094707.
23 D. Wang, D. Park, J. Griffith and A. Nowick, *Solid State Ionics*, 1981, **2**, 95–105.
24 J. Faber, C. Geoffroy, a. Roux, a. Sylvestre and P. Abélard, *Appl. Phys. A*, 1989, **49**, 225–232.
25 M. Mogensen, N. M. Sammes and G. A. Tompsett, *Solid State Ionics*, 2000, **129**, 63–94.
26 J. Koettgen, S. Grieshammer, P. Hein, B. O. H. Grope, M. Nakayama and M. Martin, *Phys. Chem. Chem. Phys.*, 2018, **20**, 14291–14321.
27 D. Marrocchelli, S. R. Bishop, H. L. Tuller and B. Yildiz, *Adv. Funct. Mater.*, 2012, **22**, 1958–1965.
28 S. Grieshammer, B. O. H. Grope, J. Koettgen and M. Martin, *Phys. Chem. Chem. Phys.*, 2014, **16**, 9974–9986.
29 B. Yildiz, *MRS Bull.*, 2014, **39**, 147–156.
30 D. Pergolesi, E. Gilardi, E. Fabbri, V. Roddatis, G. F. Harrington, T. Lippert, J. A. Kilner and E. Traversa, *ACS Appl. Mater. Interfaces*, 2018, **10**, 14160–14169.
31 E. Sediva, D. Bohdanov, G. F. Harrington, I. Rafalovskyi, J. Drahokoupil, F. Borodavka, P. Marton and J. Hlinka, *ACS Appl. Mater. Interfaces*, 2020, acsami.0c14249.
32 M. Gerstl, G. Friedbacher, F. Kubel, H. Hutter and J. Fleig, *Phys. Chem. Chem. Phys.*, 2013, **15**, 1097–1107.
33 H.-R. Kim, J.-C. Kim, K.-R. Lee, H.-I. Ji, H.-W. Lee, J.-H. Lee and J.-W. Son, *Phys. Chem. Chem. Phys.*, 2011, **13**, 6133–6137.
34 H. J. Avila-Paredes, J. Zhao, S. Wang, M. Pietrowski, R. A. De Souza, A. Reinholdt, Z. A. Munir, M. Martin and S. Kim, *J. Mater. Chem.*, 2010, **20**, 990–994.
35 M. C. Göbel, G. Gregori, X. Guo and J. Maier, *Phys. Chem. Chem. Phys.*, 2010, **12**, 14351–14361.
36 G. F. Harrington, A. Cavallaro, D. W. McComb, S. J. Skinner and J. A. Kilner, *Phys. Chem. Chem. Phys.*, 2017, **19**, 14319–14336.
37 T. C. Yeh, N. H. Perry and T. O. Mason, *J. Am. Ceram. Soc.*, 2011, **94**, 1073–1078.
38 J. Hinterberg, T. Zacherle and R. a. De Souza, *Phys. Rev. Lett.*, , DOI:10.1103/PhysRevLett.110.205901.
39 G. F. Harrington, L. Sun, B. Yildiz, K. Sasaki, N. H. Perry and H. L. Tuller, *Acta Mater.*, 2019, **166**, 447–458.
40 M. J. D. Rushton and A. Chroneos, *Sci. Rep.*, 2014, **4**, 6048.
41 R. D. Shannon and C. T. Prewitt, *Acta Crystallogr.*, 1969, **25**, 925–946.
42 M. Nakayama and M. Martin, *Phys. Chem. Chem. Phys.*, 2009, **11**, 3241.
43 A. Van Der Ven and G. Ceder, *Phys. Rev. Lett.*, 2005, **94**, 1–4.
44 S. Grieshammer, S. Eisele and J. Koettgen, *J. Phys. Chem. C*, 2018, **122**, 18809–18817.
45 T. M. Huber, A. K. Opitz, M. Kubicek, H. Hutter and J. Fleig, *Solid State Ionics*, 2014, **268**, 82–93.
46 J. P. Perdew, K. Burke and M. Ernzerhof, *Phys. Rev. Lett.*, 1996, **77**, 3865–3868.
47 G. Kresse and J. Furthmüller, *Phys. Rev. B - Condens. Matter Mater. Phys.*, 1996, **54**, 11169–11186.
48 G. Kresse and D. Joubert, *Phys. Rev. B*, 1999, **59**, 1758–1775.
49 P. E. Blöchl, *Phys. Rev. B*, 1994, **50**, 17953–17979.
50 S. Dudarev and G. Botton, *Phys. Rev. B - Condens. Matter Mater. Phys.*, 1998, **57**, 1505–1509.
51 G. Henkelman and H. Jónsson, *J. Chem. Phys.*, 2000, **113**, 9978–9985.
52 G. Henkelman, B. P. Uberuaga and H. Jónsson, *J. Chem. Phys.*, 2000, **113**, 9901–9904.
53 S. Eisele and S. Grieshammer, *J. Comput. Chem.*, 2020, **41**, 2663–2677.
54 J. Keppner, J. Schubert, M. Ziegner, B. Mogwitz, J. Janek and C. Korte, *Phys. Chem. Chem. Phys.*, 2018, **20**, 9269–9280.
55 E. Chason, *Thin Solid Films*, 2012, **526**, 1–14.
56 E. Chason and P. R. Guduru, *J. Appl. Phys.*, 2016, **119**, 191101.
57 H. Hayashi, *Solid State Ionics*, 2000, **132**, 227–233.
58 D. de Ligny and P. Richet, *Phys. Rev. B - Condens. Matter Mater. Phys.*, 1996, **53**, 3013–3022.
59 R. Huang, C. J. Kucharczyk, Y. Liang, X. Zhang, I. Takeuchi and S. M. Haile, *ACS Comb. Sci.*, 2018, **20**, 443–450.
60 J. Ahn, H. W. Jang, H. Ji, H. Kim, K. J. Yoon, J. W. Son, B. K. Kim, H. W. Lee and J. H. Lee, *Nano Lett.*, 2018, **18**, 2794–2801.
61 H. L. Tuller and A. S. Nowick, *J. Electrochem. Soc.*, 1975, **122**, 255–259.
62 H. J. Avila-Paredes, K. Choi, C.-T. Chen and S. Kim, *J. Mater. Chem.*, 2009, **19**, 4837.
63 N. Swaminathan and J. Qu, *Model. Simul. Mater. Sci. Eng.*, , DOI:10.1088/0965-0393/17/4/045006.
64 N. Yavo, D. Noiman, E. Wachtel, S. Kim, Y. Feldman, I. Lubomirsky and O. Yeheskel, *Scr. Mater.*, 2016, **123**, 86–89.
65 F. Iguchi, S. Onodera, N. Sata and H. Yugami, *Solid State Ionics*, 2012, **225**, 99–103.
66 J. Koettgen, G. Dück and M. Martin, *J. Phys. Condens. Matter*, 2020, **32**, 265402.